The atomic structure of niobium and tantalum containing borophosphate glasses

2009 J. Phys.: Condens. Matter 21 375106

(http://iopscience.iop.org/0953-8984/21/37/375106)

J. Phys.: Condens. Matter **21** (2009) 375106 (11pp) doi:10.1088/0953-8984/21/37/375106

The atomic structure of niobium and tantalum containing borophosphate glasses

K M Wetherall[1], P Doughty[1], G Mountjoy[1], M Bettinelli[2], A Speghini[3], M F Casula[4], F Cesare-Marincola[4], E Locci[4] and R J Newport[1]

[1] School of Physical Sciences, University of Kent, Ingram Building, Canterbury CT2 7NH, UK
[2] Laboratorio di Chimica dello Stato Solido, DB, Università di Verona and INSTM, UdR Verona, Strada Le Grazie 15, 37134 Verona, Italy
[3] DiSTeMeV, Università di Verona and INSTM, UdR Verona, Via della Pieve 70, 37029 Verona, Italy
[4] Dipartimento di Scienze Chimiche, Universita di Cagliari, SS 554 Bivio per Sestu, 09042 Monserrato (CA), Italy

Received 16 June 2009, in final form 24 July 2009
Published 17 August 2009
Online at stacks.iop.org/JPhysCM/21/375106

Abstract

A complete structural study has been carried out on sodium borophosphate glass containing increasing amounts of either niobium or tantalum. A combination of high energy x-ray diffraction, neutron diffraction, extended x-ray absorption fine structure, nuclear magnetic resonance, and infrared and Raman spectroscopy has been used to discern the local atomic structure of each component and the changes with M content, where M is either niobium or tantalum. The glasses are found to consist of tetrahedral borate and phosphate with octahedral MO_6. As expected, B and P play the roles of tetrahedral network formers. At low M content there are isolated MO_6 units with P···M and B···M linkages that contribute to the glass network. As the M content increases, the number of M···M links increases, and at the highest M content each MO_6 unit is connected to several others. The octahedra become significantly distorted as the niobium content increases, an effect that is not seen for tantalum.

(Some figures in this article are in colour only in the electronic version)

1. Introduction

The origin of non-linear optical (NLO) effects in glasses is a field of current interest due to their optoelectronic application. For example, glasses with elevated NLO effects are promising candidates for ultrafast optical switches [1]. Large values of NLO susceptibility $\chi^{(3)}$ are observed in glasses containing empty d shell transition metal ions such as Ti^{4+} and Nb^{5+} [2]. One such group of glasses are sodium borophosphates containing niobium or tantalum, with the composition $xM_2O_5(1-x)(Na_2B_4O_7)_{0.05}(1-x)(NaPO_3)_{0.95}$, where M^{5+} is either Nb^{5+} or Ta^{5+} ions. NLO effects in these glasses have recently been investigated, with the aim of explaining the phenomena in terms of the local atomic environment of Nb^{5+} and Ta^{5+} ions [3–6]. However, there have been very few studies of the structure, in particular of the Nb or Ta environments.

Given the interest in the NLO properties of these glasses, there have been several previous attempts to characterize the atomic structure that mainly utilize vibrational spectroscopy. Previous spectroscopic studies of Nb_2O_5–$NaPO_3$–$Na_2B_4O_7$ glasses have shown that as the M^{5+} concentration is increased, its role changes [7]. When M_2O_5 is added in small quantities it forms isolated MO_6 octahedra. As the concentration is increased there begins to be corner sharing of octahedra. Eventually, at the highest content, a three-dimensional network of corner sharing MO_6 takes on the role of a network former, strengthening the glass network by eliminating non-bridging oxygen atoms [7]. Previous studies have indicated that this clustering of the MO_6 octahedra results in the

Table 1. Glass compositions, the label indicates the mol% M_2O_5. A reasonable estimate of error in these values is ±2%.

Sample	M_2O_5 (mol%)	$Na_2B_4O_7$ (mol%)	$NaPO_3$ (mol%)	Fe_2O_3 (mol%)	Density (g cm^{-3})	Density (atoms Å^{-3})
Ta 9.3	9.3	4.4	84.3	2.0		
Ta19.6	19.6	3.9	74.5	2.0	4.04	0.0799
Ta35.0	35.0	3.2	59.8	2.0	4.70	0.0747
Nb10.8	10.8	4.6	84.1	0.5		
Nb21.1	21.1	4.7	73.7	0.5	2.92	0.0720
Nb36.5	36.5	3.2	59.8	0.5	3.48	0.0759

increase in the third order non-linear susceptibility due to the hyperpolarizability of an extended structure of MO_6 units [7]. In particular, the short M–O bond is important as it increases the influence of the d orbitals on the non-linear optical response of the glass.

The conclusions above have been drawn from spectroscopic techniques that observe the movement of the bonds rather than direct observation of the correlations in positions between M^{5+} ions and neighbouring ions. There have also been extended x-ray absorption fine structure (EXAFS) [7] and x-ray diffraction (XRD) [8] studies reported on glasses with the same composition as those studied here, and nuclear magnetic resonance (NMR) [9] has been performed on related but simpler glass compositions. Presented here if a full study of the atomic-scale structure that uses data taken some time ago. It includes the techniques of high energy x-ray diffraction (HEXRD), neutron diffraction (ND) and NMR which are new to the literature on these glasses, as well as EXAFS, Raman and IR spectroscopy data not previously published.

2. Method

2.1. Glass preparation

Glasses were made with batched compositions listed in table 1. They contain small amounts of iron for the purposes of the Mossbauer study presented in [5]. As the Fe content is less than 1/3rd of B content, Fe is neglected in the present study. The glasses were prepared by following the method described in [5]. Analytical grade Nb_2O_5, Ta_2O_5, $Na_2B_4O_7{\cdot}H_2O$, $NaH_2PO_4{\cdot}H_2O$ and $Fe(NO_3)_3$ for the niobium containing glass and Fe_2O_3 for the tantalum containing glass were used. The appropriate mixtures were melted in an electric furnace under oxygen in a platinum crucible at 1250 °C for 30 min. The melts were quenched by pouring on to a cold copper plate at room temperature and annealed overnight under an oxygen atmosphere, for further details see [5]. Their densities were measured using Archimedes' method and are also listed in table 1.

2.2. Raman and IR spectroscopy

Raman spectra were measured using a Jobin Yvon model HR640 Raman spectrometer, fitted with a 25 mW, 623.8 nm helium neon laser and a liquid nitrogen cooled CCD multichannel detector. Repeated measurements with improved resolution and less noise were taken for the samples containing 9.3% Ta, 35.0% Ta and 36.5% Nb using a LabRAM 300 system configured with a 50 mW 532 nm laser excitation. Spectra were recorded by a TE air cooled CCD detector cooled to −70 °C. (Comparison between the two measurements showed the peak positions and heights were consistent.)

Infrared spectra were measured by a Biorad FTS175C spectrometer controlled by WinIR software. Samples were diluted in dry KBr and measured for 64 scans in diffuse reflectance mode over the range 4000–400 cm^{-1} with a resolution of 4 cm^{-1}. The spectrum of blank KBr was also measured to allow background subtraction. As the spectrum for the glass containing 21.1% Nb_2O_5 was recorded at a later date, the background has a slight influence from adsorbed water around 1500 cm^{-1}.

2.3. High energy x-ray diffraction measurements

The x-ray diffraction data was collected on Station 9.1 of the synchrotron radiation source (SRS), Daresbury Laboratory. The finely powdered samples were enclosed inside a 0.5 mm thick circular aluminium annulus with kapton windows. They were mounted in $\theta/2\theta$ flat plate transmission geometry with scanning of 2θ from 2° to 126°. The incident beam size was 1 mm × 10 mm. For the samples containing tantalum, the x-ray wavelength was set at $\lambda = 0.4858$ Å (calibrated using the K-edge of a Ag foil); this wavelength provides data to a high value of wavevector transfer ($Q_{max} \sim 23$ Å^{-1} where $Q = 4\pi \sin\theta/\lambda$). For the samples containing niobium, the wavelength had to be changed to 0.6569 Å (again calibrated using the K-edge of a Ag foil) to avoid fluorescence. An ion chamber detector was used with a 1 mm slit at 30 cm to retain acceptable resolution.

The first stage of the data analysis is the application of corrections for the polarization of the x-ray beam, the variation in sample thickness with incident angle, and background scattering. Corrections for the absorption, Compton scattering, the self-scattering and the sharpening function (where the signal is divided by the average form factor per electron squared) are then made. The resultant scattering intensity, $i(Q)$ reveals structural information *via* a Fourier transform to obtain the total pair correlation function, as in (1).

$$T_X(r) = 2\pi^2\rho_N r + \int_{Q_{min}}^{Q_{max}} M(Q)\,Q i_X(Q)\sin(Qr)\,\mathrm{d}Q \quad (1)$$

where r is the atomic separation between atom pairs, ρ_N is the bulk number density and $M(Q)$ is a window function applied to reduce the Fourier transform termination artefacts that arise

from the finite range of Q. A Hanning window function has been used here.

In order to obtain the structural information directly from the experimental data, each possible pairwise combination of elements i and j is represented by a pair correlation function $p_{ij}(r)$ that is then fitted to the data. The Q space simulation of each pair correlation function $p_{ij}(Q)$ is generated using (2).

$$p_{ij}(Q) = N_{ij}\omega_{ij} \sin Qr_{ij} \exp[-0.5Q^2\sigma_{ij}^2](c_j Qr_{ij})^{-1}. \quad (2)$$

The sum of these $p_{ij}(Q)$ is equivalent to the $i_X(Q)$ in (1) and is Fourier transformed using (1) for comparison to the experimental real space data $T_X(r)$, having been subjected to exactly the same Fourier transform effects.

The parameters in (2) are the averaged coordination number of atom type j around an atom of type i, N_{ij}, the pairwise atomic separation, r_{ij}, and the disorder factor (a measure of thermal and static disorder) σ_{ij}. These are varied in the fitting procedure. The parameter c_j is the concentration of atom type j and ω_{ij} is the weighting function that accounts for the variation in scattering strength $f_i(Q)$ of different atom types, as defined in (3).

$$\omega_{ij} = \frac{(2-\delta_{ij})c_i c_j f_i(Q) f_j(Q)}{[\overline{f(Q)}]^2}. \quad (3)$$

2.4. Neutron diffraction measurements

The neutron diffraction data was collected on the GEM diffractometer on the ISIS spallation neutron source at the Rutherford Appleton Laboratory, UK. Time-of-flight data was collected over a wide range of Q (up to 40 Å^{-1}). The powdered samples were placed in an 8.3 mm vanadium can. The data was analysed using the ATLAS suite of programs [10]. An additional correction was made to the data from the sample containing 19.6% Ta_2O_5 as an insufficient amount of sample in the vanadium can meant the sample did not fill the vertical height of the beam (a polynomial was subtracted from the low Q part of the Q-space data).

The principles of neutron diffraction have much in common with those for x-rays, and equations of the same form are used in the analysis. A key difference originates from the neutron's interacting with nuclei as scattering centres rather than electron density as for x-rays. In neutron diffraction the real space total correlation function $T(r)$ is given by (4), where b_i is the scattering length that describes how strongly the target nuclei scatter neutrons. The value of b_i used for a given element is an average over the natural abundance of isotopes for that element. Here a Lorch window function is used.

$$T_N(r) = 4\pi\rho_N r\left(\sum_i c_i b_i\right)^2 + \frac{2}{\pi}\int_{Q_{\min}}^{Q_{\max}} M(Q)Qi_N(Q)\sin(Qr)\,\mathrm{d}Q. \quad (4)$$

Structural information is then obtained from the experimental data using the same method as for the x-ray diffraction data. Each type of atom pair is modelled by a pair correlation function as defined in (2). For neutron diffraction the weighting factors are defined in (5).

$$\omega_{ij} = (2-\delta_{ij})c_i c_j b_i b_j. \quad (5)$$

The accuracy of information obtained from fitting pair correlation functions depends on correctly assigning the atom types to i and j for all the peaks $p_{ij}(r)$, including those that overlap. Accurate results can be obtained once all peaks are identified and accounted for. The fitting was then optimized by using a non-linear least squares fitting algorithm to find the parameters R_{ij}, N_{ij} and σ_{ij} which give best agreement with experiment [11].

2.5. X-ray absorption measurements

The EXAFS data was collected on Station 9.2 of the Synchrotron Radiation Source (SRS), Daresbury Laboratory. The spectra were recorded in transmission mode using a double-crystal Si(220) monochromator, and ionization chambers to detect the incident and transmitted beam intensities, I_0 and I_t, respectively. Data were recorded around the Ta L_{III} edge at 9881 eV before changing to the Nb K-edge at 18 986 eV. Finely ground samples were diluted with polyethylene and pressed into pellets to give a satisfactory absorption and edge absorption step. The monochromator was adjusted to give 50% harmonic rejection. The EXAFS spectra were collected over the range k = 3–18 Å^{-1} with a step of 0.045 Å^{-1}, where k is the photoelectron wavevector. Multiple spectra were recorded and summed for each sample. The programs EXCALIB, VIPER and EXCURV98 were used to analyse the data [12]. The k^3-weighted EXAFS signal is fitted by structural parameters to obtain values for coordination number, N, interatomic distance, R, and the Debye–Waller factor, $A = 2\sigma^2$. The magnitude of the EXAFS, $\chi(k)$, is:

$$\chi(k) = AFAC\sum_j \frac{N_j}{kR_j^2}|f(\pi,k,R_j)|\mathrm{e}^{-2R_j/\lambda(k)}\mathrm{e}^{-2\sigma_j^2k^2} \times \sin(2kR_j + 2\delta(k) + \psi(k,R_j)) \quad (6)$$

where $f(\pi,k,R_j)$ describes the photoelectron backscattering, $\lambda(k)$ is the electron mean free path, and $\delta(k)$ and $\psi(k,R_j)$ are the phaseshifts experienced by the photoelectron due to the potentials of the emitting and backscattering atoms respectively. *AFAC* is the proportion of electrons that are scattered elastically and is refined by analysis of reference materials with known structure, i.e. M_2O_5. Least squares refinements of the structural parameters were carried out against the k^3-weighted EXAFS signal to minimize the fit index, FI, as in (7).

$$\mathrm{FI} = \sum_i (k^3(\chi_i^{\mathrm{T}} - \chi_i^{\mathrm{E}}))^2 \quad (7)$$

where χ_i^{T} and χ_i^{E} are the modelled theoretical and experimental EXAFS, respectively. The results of the refinements are reported in terms of the discrepancy index, R_{di}.

$$R_{\mathrm{di}} = \frac{\int|(\chi^{\mathrm{T}}(k) - \chi^{\mathrm{E}}(k))|k^3\,\mathrm{d}k}{\int|\chi^{\mathrm{E}}(k)|k^3\,\mathrm{d}k} \times 100\%. \quad (8)$$

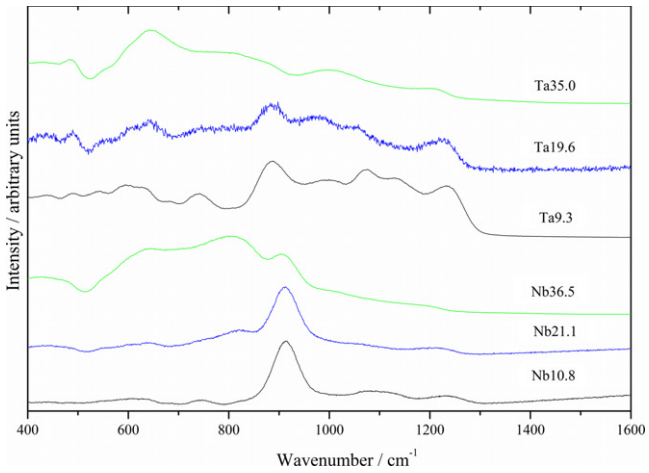

Figure 1. Raman spectra showing evolution of the peaks as a function of Ta and Nb content.

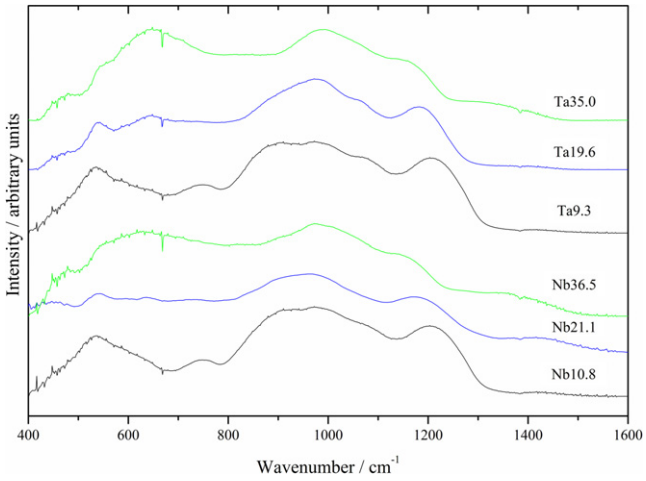

Figure 2. IR spectra showing evolution of the peaks as a function of Ta and Nb content.

2.6. NMR measurements

Solid-state NMR experiments were performed at 9.39 T using a Varian 400 UNITY INOVA spectrometer operating at the Larmor frequency of 161.90 and 128.32 Hz for ^{31}P and ^{11}B, respectively, and equipped with a 4 mm probe head. The samples were packed into cylindrical Si_3N_4 rotors. All spectra were recorded under magic angle spinning (MAS) conditions at a spinning speed of 12 kHz.

The ^{31}P MAS experiments were run with a pulse length of 5 μs (90° tip angle), a recycle time of 1 s, 120 kHz bandwidth, and 512 scans. ^{31}P chemical shifts were referenced to 85% H_3PO_4 at 0 ppm. The ^{11}B MAS spectra were obtained using a short pulse of 1.2 μs, a recycle time of 1 s, 100 kHz bandwidth, and 2048 scans. The pulse length was chosen to be 1/6 of the $\pi/2$ pulse length, calibrated using a 1 M H_3BO_3 aqueous solution. ^{11}B chemical shifts were referenced to aqueous boric acid which resonates at 19.6 ppm relative to boron trifluoride etherate.

3. Results

3.1. Raman and IR spectroscopy

The spectra recorded from all six samples are shown in figures 1 and 2, the peak positions are listed in table 2. The spectra exhibit the anticipated features as are highlighted in the literature [2, 5, 7, 8]. At the lowest M_2O_5 content, a feature at 900 cm^{-1} is dominant that is assigned as isolated MO_6 octahedra. As the concentration increases this band decreases significantly and the dominant feature becomes a band at 810 cm^{-1} that relates to corner sharing octahedral chains. There is a strong secondary feature around 650 cm^{-1} that implies a three-dimensional network of MO_6 octahedra is beginning to form. This interpretation is consistent with the identification of phosphate bands. A band at 1270 cm^{-1} and an intense but broad band between 1050 and 1120 cm^{-1}, which both decrease, indicate a shortening of the meta-phosphate chains, and a band at ∼980 cm^{-1}, which increases, indicates an increase in isolated PO_4 units.

These assignments are further reinforced by the comparison of the Nb and Ta samples. Bands that experience a shift in frequency and a difference in intensity between the Nb and Ta samples almost certainly involve an M–O bond vibration, whereas bands which do not change with M type probably have a different origin. This is particularly evident with the band at 910 cm^{-1} as it is much stronger in the niobium samples than in the tantalum samples (where it appears at 890 cm^{-1}). This is because, within the octahedra of NbO_6, the niobium is able to move off-centre, giving rise to a large variation in Nb–O bond lengths. There is therefore a much larger resonance with the stretching vibration occurring at 910 cm^{-1}. This shows the greater degree of distortion that occurs within the niobium octahedra compared to that found within the tantalum octahedra.

Bands have been assigned to Q^0, Q^1 and Q^2, where Q^n defines the connectivity of the phosphate units by n bridging oxygen atoms. Q^0 is therefore isolated PO_4 tetrahedra, Q^1 are dimers and Q^2 are chains. The identification of all three types implies that there is complexity in the P connectivity: there are vibrations occurring in the sample that are present in the phosphate units connected to two, one or no other phosphate units. The presence of all three types of band suggests that P is connected to network-forming units other than phosphate.

3.2. High energy x-ray and neutron diffraction measurements

The $i(Q)$ data for the four samples Ta19.6, Ta35.0, Nb21.1 and Nb36.5 from neutron and x-ray diffraction are shown in figure 3. The corresponding $T(r)$ is shown in figure 4 for neutron and x-ray diffraction. Table 3 shows the sequence of interatomic correlations (between atom types i and j) that was used to fit the x-ray and neutron diffraction data simultaneously to obtain a single set of structural parameters for each sample that agree with both techniques. The values obtained by the fitting are listed in the table as R, the pairwise interatomic distance, N, the number of neighbouring atoms, and σ, the standard deviation in distance.

Multi-component systems such as these are complex to model with individual pair correlations due to the presence of overlapping correlations at r values greater than ∼3 Å. It

Table 2. Positions (cm^{-1}) and assignments of IR and Raman bands, to the nearest 5 cm^{-1}. Notation used is as follows: w: weak; m: medium; b: broad; sh: shoulder; s: strong.

Samples containing Nb_2O_5						Samples containing Ta_2O_5							
10.8 mol%		21.1 mol%		36.5 mol%		9.3 mol%		19.6 mol%		35.0 mol%			
Raman	FTIR	Raman	FTIR	Raman	FTIR	Raman	FTIR	Raman	FTIR	Raman	FTIR	Assignments	Trend with increasing M content
210_{w}				$230_{s,b}$		$210_{m,b}$		$250_{s,b}$		210_{s}		O–Nb–O	Increasing
445_{w}		455_{b}		$445_{m,b}$		440_{w}		435_{w}		420_{w}		MO_6 octahedra	Increasing
			445_{w}		$480_{m,sh}$	495_{w}		490_{w}	475_{sh}	485_{w}	480_{w}	PO_4 tetrahedra	Increasing
	535_{s}	555_{w}	540_{m}		$560_{m,sh}$	545_{w}	535_{s}	555_{w}	540_{m}	$560_{w,s}$	$555_{m,sh}$	M–O bond	Decreasing
$620_{m,b}$	$620_{b,sh}$	640_{w}	640_{w}	640_{s}	630_{s}	630_{m}		640_{m}	645_{m}	645_{s}	650_{s}	cross-linked MO_6	Increasing
745_{m}	750_{m}	760_{sh}	$730_{w,b}$			745_{m}	745_{m}	740_{b}				P–O–P bridge	Decreasing
		820_{m}		805_{s}				800_{w}		$790_{m,b}$		Corner shared MO_6	Increasing
$910_{s,sh}$	925_{s}	$910_{s,sh}$	$915_{s,sh}$	$905_{m,sh}$	$905_{m,sh}$	890_{s}	905_{m}	885_{s}	890_{sh}			Isolated MO_6 and P-P bridge	Decreasing
	975_{m}		965_{s}		970_{s}		975_{s}		975_{s}		990_{s}	isolated PO_4	Increasing
1100_{m}	1070_{sh}	$1060_{w,b}$				1075_{s}	1065_{m}	1050_{w}	1060_{sh}			Q^1 & Q^2	Decreasing
1230_{m}	1205_{s}	$1215_{w,b}$	1190_{m}	$1200_{w,sh}$	1170_{w}	1235_{s}	1205_{s}	1225_{m}	1180_{m}	$1205_{w,b}$	1160_{w}		Decreasing

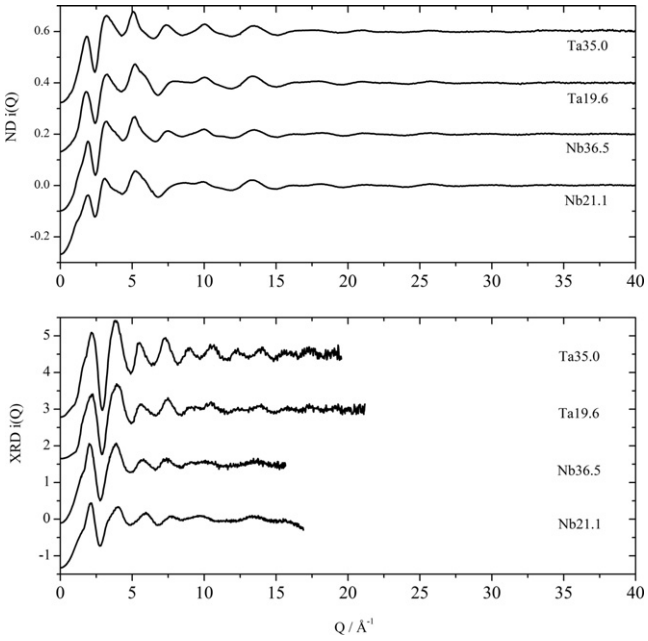

Figure 3. The Q-space interference function, $i(Q)$, obtained from neutron diffraction (above) and from x-ray diffraction (below).

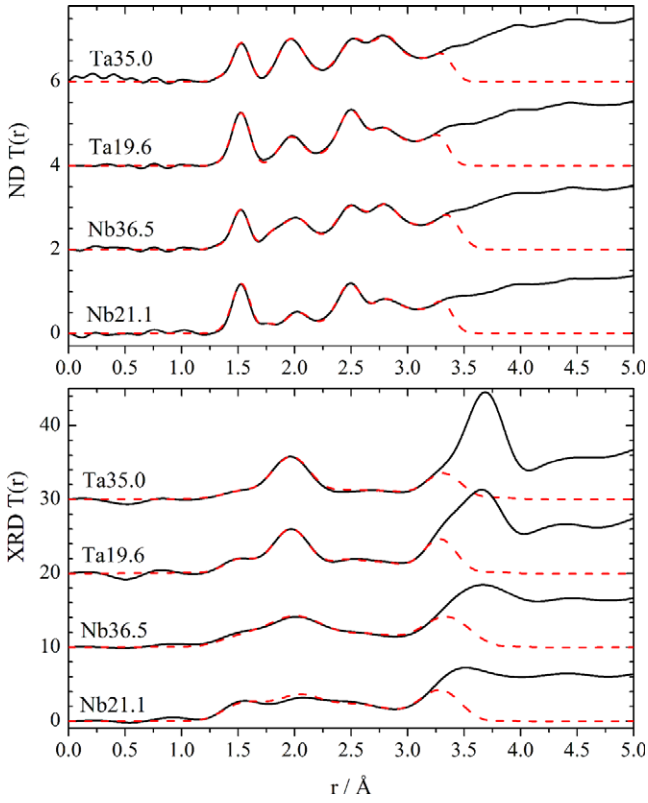

Figure 4. The total pair distribution function, $T(r)$, (solid line) together with the fit (dashed line) from the neutron diffraction (above) and from the x-ray diffraction (below).

is therefore only possible reliably to assign correlations up to ∼3 Å. (Note that a final, non-fitted, peak is used to account for the background from neighbouring correlations at high r.) Neutron and x-ray diffraction have different weightings for any given element. In the neutron diffraction data the prominent features are from correlations involving oxygen and phosphorus, whereas in x-rays they are from niobium or tantalum. Combining the techniques therefore allows the more robust identification of each pair correlation type and hence is an excellent way of ensuring the sequence of correlations used is correct.

The first interatomic correlation is B–O at ∼1.40–1.45 Å, visible as a shoulder on the low r side of the first peak in the neutron data. The B is coordinated to four Os, as also observed in the NMR results (see section 3.4). Typically, four-fold coordinated boron has a bond length of 1.48 Å whilst three-coordinated boron has a bond length of 1.37 Å. The shortening of the interatomic distance by 0.03–0.04 Å, as the concentration of niobium or tantalum is increased suggests the appearance of some three-fold coordinated B. The second

Table 3. Structural parameters obtained from the simulations of x-ray and neutron diffraction data. Note that reasonable estimates of errors are ±0.02 Å in R, ±15% in N and ±0.01 Å in σ.

Sample	Correlation	R (Å)	N	σ (Å)
Ta19.6	B–O	1.44	4.0	0.05
	P–O	1.54	4.1	0.05
	Ta–O	1.96	6.1	0.09
	Na–O	2.31	4.1	0.17
	O–(B/P)–O	2.50	3.3	0.09
	O–(M)–O	2.80	4.1	0.13
Ta35.0	B–O	1.41	4.0	0.07
	P–O	1.54	3.9	0.05
	Ta–O	1.97	6.0	0.10
	Na–O	2.32	4.0	0.16
	O–(B/P)–O	2.53	3.1	0.11
	O–(M)–O	2.82	4.1	0.11
Nb21.1	B–O	1.46	3.9	0.08
	P–O	1.54	3.9	0.06
	Nb–O	1.75	0.9	0.04
	Nb–O	2.03	4.9	0.11
	Na–O	2.37	3.4	0.11
	O–(B/P)–O	2.50	3.0	0.09
	O–(M)–O	2.82	3.9	0.14
Nb36.5	B–O	1.42	4.0	0.08
	P–O	1.53	3.9	0.05
	Nb–O	1.79	0.9	0.07
	Nb–O	2.02	4.9	0.13
	Na–O	2.37	3.3	0.11
	O–(B/P)–O	2.51	3.0	0.11
	O–(M)–O	2.81	4.2	0.12

correlation is P–O at 1.54 Å; this is the first significant feature in the neutron data and a shoulder in the x-ray diffraction data. The P is coordinated to four Os, as expected. The next correlation is due to Ta–O or Nb–O at ∼2 Å, this is the first prominent feature in the x-ray data. The Nb–O correlation has a large spread in bond distance, ranging from 1.75 to 2.05 Å (as is found in the EXAFS data, see section 3.3). The relatively short Nb–O bond, fitted at 1.75 Å, is often found for NbO_6 octahedra in crystals [13]. Both the Nb and Ta are coordinated to a total of approximately six oxygen atoms.

The next correlation to be fitted is Na–O at ∼2.3 Å. This peak is completely overlapped and is only visible as a broad shoulder to the low r side of the O–O peak. There is therefore an increased uncertainty in the fitted parameters and a relatively limited amount of information can be gained on the Na site. The bond length is typical of Na–O whilst the coordination can only be constrained to be being between 3 and 4.5.

The region from 2.5 to 2.8 Å is dominated by the O···O interatomic correlation. In the neutron data there are two distinguishable peaks that have been modelled with two correlations. The first peak at 2.5 Å originates from the O–(P)–O and the O–(B)–O distance. The second peak at 2.8 Å is from the O–(Nb/Ta)–O distance. There is not expected to be an O–(Na)–O correlation at distances less than 3.0 Å because the Na–O bond length of ∼2.3 Å is significantly longer than B–O, P–O or M–O bond lengths.

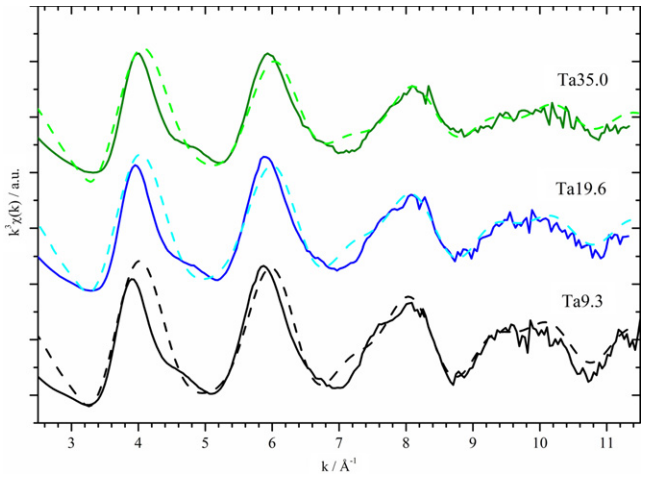

Figure 5. Ta L_3-edge k^3 weighted EXAFS data of samples containing increasing amounts of Ta. The solid lines are the experimental data and the dashed lines are the theoretical fits.

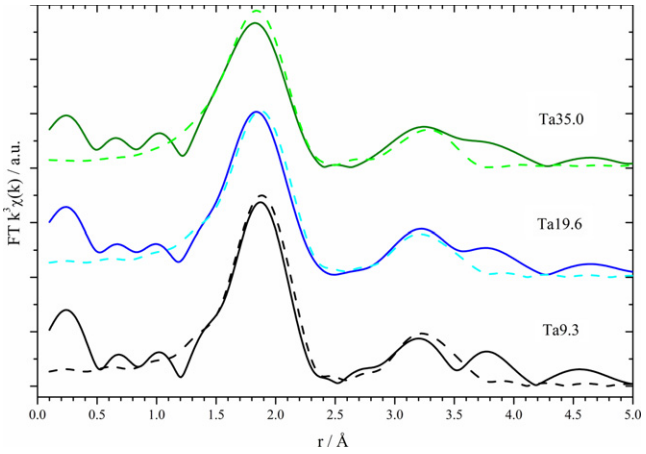

Figure 6. The Fourier transform of the Ta L_3-edge k^3 weighted EXAFS data of samples containing increasing amounts of Ta. The solid lines are the experimental data and the dashed lines are the theoretical fits.

3.3. X-ray absorption measurements

The following EXAFS results were obtained using an *AFAC* value of 0.8766, found by fitting the crystal Ta_2O_5. The EXAFS spectra and corresponding fits for the Ta samples are shown in figure 5 in k space and in figure 6 the Fourier transforms of the EXAFS spectra are shown. The EXAFS spectra for the Nb samples are shown in figure 7 in k space and in figure 8 in real space. EXAFS results are generally accepted to be accurate to ±0.02 Å for the atomic separation, R, however the coordination number, N, is only accurate to ±20%. There is a close relationship between N and the Debye–Waller factor, A, that means either parameter can only be measured if the other is fixed based on structural information from another source. The results of the fitting are shown in table 4. The coordination numbers of the first correlation were fixed at a value that is consistent with previous results and that gave realistic values for A. The coordination number of the second correlation was allowed to vary whilst

Table 4. Ta L_3-edge EXAFS derived structural parameters. Reasonable estimates of errors are ±0.02 Å in R, ±20% in N and ±0.003 Å^2 in A. Note parameters in italics have been fixed during the fitting process.

	Ta 9.3			Ta 19.6			Ta 35.0		
Interatomic correlation	R (Å)	N	A (Å^2)	R (Å)	N	A (Å^2)	R (Å)	N	A (Å^2)
Ta–O	1.98	*6*	0.016	1.98	*6*	0.020	1.96	*6*	0.024
Ta···P	3.31	3.0	*0.013*	3.29	2.5	*0.013*	3.30	2.1	*0.013*
R_{di} (%)		38.3			36.2			36.5	

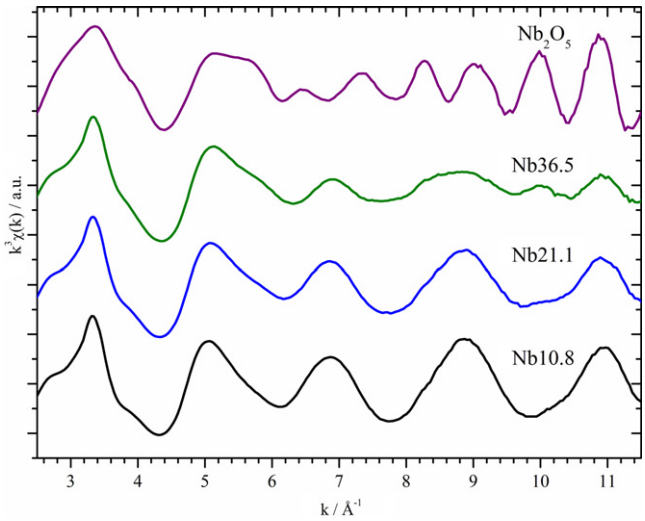

Figure 7. Nb K-edge k^3 weighted EXAFS data of samples containing increasing amounts of Nb and of the reference material Nb_2O_5.

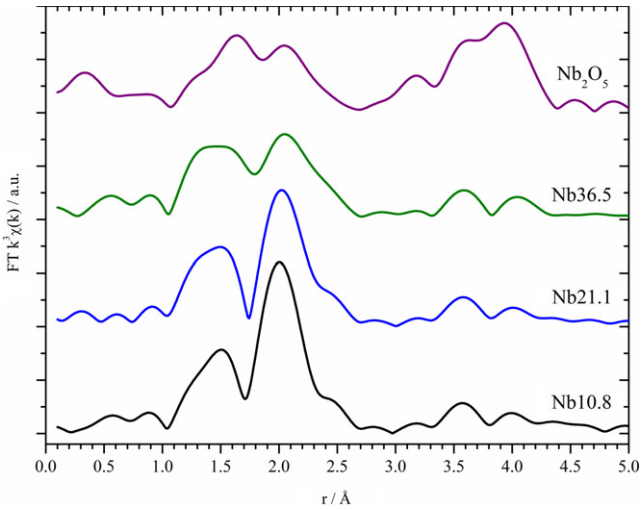

Figure 8. The Fourier transform of the Nb K-edge k^3 weighted EXAFS data of samples containing increasing amounts of Nb and of the reference material Nb_2O_5.

A remained constant. This is to enable us to see the trend in coordination that is otherwise masked by the effects of overlapping correlations at high r.

The Nb and Ta spectra look very different due to the difference in distortion in the Nb and Ta octahedra. The Ta samples have typical EXAFS spectra with a peak around 2 Å due to the Ta–O correlation and two peaks between 3 and 4 Å due to a combination of Ta···P, Ta···B, Ta···Ta or Ta···Na correlations. The observed Ta–O distance of 1.98 Å is typical for Ta in 6-fold coordination. The Ta–O coordination number can also be checked by dividing the total valence of Ta (5+) by the average bond valence, calculated using (9) [14].

$$v_{\mathrm{Ta-O}} = \exp\left(\frac{1.920\ \text{Å} - R_{\mathrm{Ta-O}}}{0.37\text{Å}}\right). \tag{9}$$

For a coordination of 6, the calculated total valence is between 5.13 and 5.44, this is within 9% of the expected valence of 5, hence reinforcing the assignment of 6-fold coordination.

There are two peaks clearly visible at high r: the first is likely to be from Ta···P and/or Ta···B correlations, and the second is likely to be from Ta···Ta or Ta···Na correlations. It is not possible to gain accurate information on the interatomic distance and coordination when so many correlations overlap, therefore only the first peak at high r has been fitted. It shows that the Ta has neighbours which are P and/or B at a length of ∼3.3 Å. The number of P and/or B neighbours decreases with increasing M content, since it becomes more likely that an M atom will have M neighbours. The second peak at high r shifts to a lower atomic separation with increasing M content. As the Ta···Ta atomic separation is smaller than the Ta···Na this shift indicates an increase in the Ta···Ta coordination with increasing M content.

The Nb samples give much more complicated EXAFS spectra and Fourier transforms as shown in figure 8. At low Nb concentration the low r spectra consists of a small peak around 1.5 Å and a much larger peak around 2 Å. This can be associated with the results from vibrational spectroscopy which suggested that, within the octahedra of NbO_6, the niobium is able to move off-centre. As the concentration increases, the second peak decreases and becomes a very broad feature. Comparison to niobium crystals shows that the EXAFS at higher Nb concentration resembles that of Nb_2O_5 [15–17]. The observed EXAFS features may be associated with a high degree of distortion within the NbO_6 octahedra, giving rise to a large variation in Nb–O bond lengths. Several studies suggest that there is a high degree of destructive interference of the backscattered electron waves due to this large range of Nb–O distances, leading to more ill-defined peaks in the Fourier transform of $\chi(k)$ [17, 16, 15]. For the samples studied here, this implies that at low Nb concentration the octahedra have a fairly regular shape and that as the Nb concentration is increased the shape of the octahedra become more variable and distorted, until they resemble the octahedra in a pure Nb_2O_5 system.

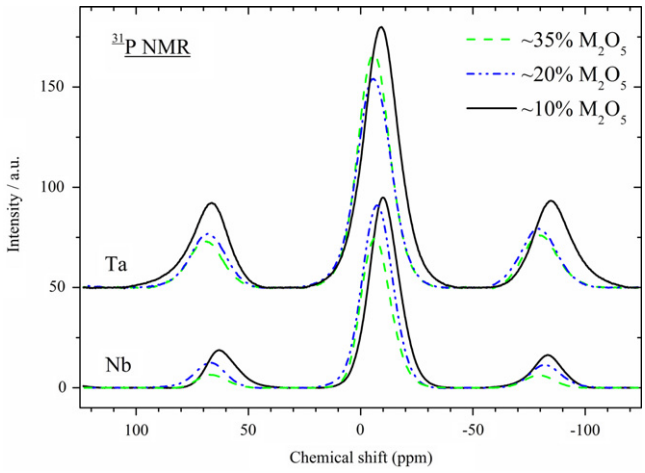

Figure 9. ^{31}P MAS NMR spectra for all samples containing increasing amounts of Ta or Nb.

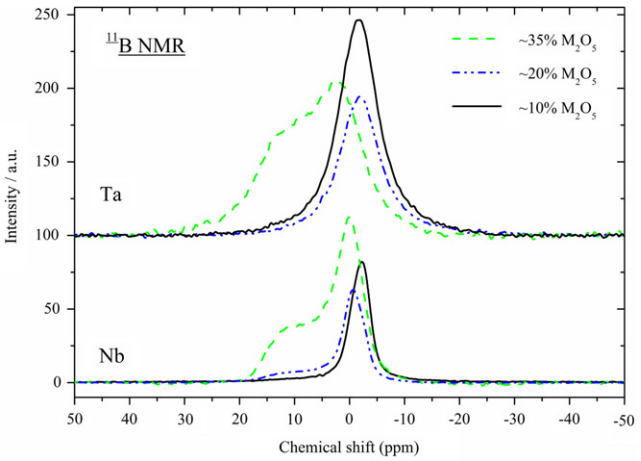

Figure 10. ^{11}B MAS NMR spectra for all samples containing increasing amounts of Ta or Nb.

Table 5. ^{31}P and ^{11}B MAS NMR chemical shifts. sh designates a shoulder.

Sample	δ_P (ppm)	δ_B (ppm)
Ta 9.3	−9.3	−1.7
Ta 19.6	−5.8	0.4
Ta 35.0	−6.0	2.8
		sh ∼ 10
Nb 10.8	−9.9	−2.2
Nb 21.1	−7.3	−0.6
		sh ∼ 12
Nb 36.5	−6.6	−0.003
		sh ∼ 12

There are two peaks in the high r region between 3.5 and 4.5 Å, each ∼0.5 Å higher than in the Ta EXAFS. The relationship between this distance and the associated bond angle around the oxygen means that the peak around 3.6 Å can only be assigned to Nb···P for Nb–O bond lengths greater than 2.1 Å. Similarly the peak around 4 Å can only be assigned to Nb···Nb for Nb–O bond lengths greater than 2.1 Å (although this peak will also have a contribution due Nb···Na correlations).

3.4. NMR measurements

The measured chemical shifts are shown in table 5 for both the ^{31}P and ^{11}B MAS NMR, and the spectra are shown in figures 9 and 10 respectively. As these samples contain more than one network former, the NMR results are relatively complex to interpret. NMR studies of simple borophosphate glasses [18] have shown that the typical Q speciation assigned to the chemical shifts is affected by the number of P–O_B–B links, where O_B is bridging oxygen. The notation we shall use herein is $P^m_{(n)}$, where m is the number of bridging oxygen atoms and n is the number of links to network formers other than P. It is found that the chemical shifts of a normal Q^n species is shifted by $\sim +10$ ppm if one of the O_B is linked to a network former other than P. Studies of mixed network sodium–niobium phosphate glasses [9] have shown a similar difference in the chemical shift due to the addition of niobium. This means that in the glasses studied here, n can indicate links to B or Nb (and similarly for Ta).

By comparing to the results of [18] and to the published chemical shifts associated with the different Q^n species in phosphates, the ^{31}P NMR chemical shifts can be assigned as either $P^2_{(1)}$, $P^2_{(2)}$ or $P^3_{(3)}$. This range of Q^n species is consistent with the vibrational spectroscopy results, which showed evidence both of P–O–P links and of isolated PO_4 units. The slight increase in chemical shift with Ta/Nb concentration indicates an increase in the links to other network formers and hence a breakdown of the P–O–P network, as is also shown by the disappearance of the P–O–P link and the increase of isolated PO_4 in the vibrational spectroscopy. Using a notation analogous to that adopted for P, the ^{11}B NMR chemical shifts are assigned as $B^4_{(4)}$ and the shoulder that appears at higher Ta/Nb concentration is three-fold coordinated B. This is consistent with the shortening of the B–O distance at higher Ta/Nb concentration which was observed in the diffraction results.

4. Discussion

By drawing together all the data it is possible to construct a detailed picture of this complex glass structure, first by looking at each local structural unit and then by considering the connectivity between these components. At low M^{5+} concentration the boron is mostly coordinated to four oxygen atoms. As the concentration of M^{5+} increases there is a noticeable shift to three-fold coordinated boron as shown by the NMR and the shortening of the B–O bond length. This higher M^{5+} content requires more connectivity to M^{5+}, thereby restricting the connections available to the boron and forcing it to reduce its coordination. The reduction of B coordination from 4 to 3 is also seen in borate glasses with high metal cation content [19]. Three-fold coordinated boron sites are less stable due to an unoccupied 2p electron orbit, so the appearance of this site with increasing M^{5+} content may reduce the stability of the borophosphate network.

The phosphate units observed here are typical of the anticipated tetrahedral units, as shown by the P–O and O–(P)–O bond lengths and the corresponding average tetrahedral angle of 109°. The NMR gives evidence of PO_4 units in the form $P^2_{(1)}$, $P^2_{(2)}$ and $P^3_{(3)}$. A reasonable description is that a typical PO_4 unit has zero or one bridging oxygen to another phosphate unit, i.e. P–O–P, and one, two or three bridging oxygen to either B or M^{5+}, i.e. P–O–B or P–O–M. The coordination of P is completed by the non-bridging oxygen atoms, which would typically number two per PO_4 unit.

The presence of non-bridging oxygen atoms (O_{nb}) is expected as the glass contains Na, which has a known role as a network modifier. Na reduces the number of linkages in glass networks by introducing O_{nb} [20]. The diffraction results estimate the Na–O bond length as between 2.31 and 2.37 Å, which suggests a coordination between 4.0 and 4.7. The fitted coordination of 4 is therefore reasonable, to within the experimental and fitting uncertainty. The sodium is bonded to O_{nb} to maintain charge balance.

Both the Nb and Ta are coordinated to six oxygen atoms, as confirmed by the HEXRD/ND fitting of coordination number and bond length, and the vibrational spectroscopy features associated with MO_6 octahedra. The valence is calculated using (9) and is found to be within 10% of the expected value of +5, reinforcing the assignment of 6-fold coordination. The O–M–O length also gives an average O–M–O angle of 91° as expected for an octahedral structure.

The Ta is in a well ordered site; however, at low M content, there is a tendency for Nb to be in an off-centre position within the octahedra. The shape of the octahedra becomes progressively more distorted at higher Nb content, as shown by the variation in Nb–O bond lengths. Nb starts off in isolated NbO_6 units, but as the concentration increases the Nb begins to have more Nb neighbours. The local atomic environment around Nb then starts to have similarities to that of Nb in Nb_2O_5, which is composed of distorted octahedra. The EXAFS spectra of the samples also show the Nb environment becomes increasingly similar to that of the crystal. This can be further understood by considering the linkages to the Nb octahedra. At low Nb content the Nb octahedra are linked to P or B rather than to other Nb, and are constrained into well ordered octahedra by well-defined P–O bond lengths. As the Nb content increases, so does the number of Nb···Nb connections whilst the number of Nb···P/B decreases; there is therefore more variability in the Nb–O bond lengths leading to more distorted octahedra.

The connectivity of such a complex glass is not easily determined experimentally but it can be modelled if sufficient information is available. Based on the experimental evidence gathered here, the following can be proposed for the typical connectivity.

- Each B has four B···P/M linkages.
- Each P has zero or one P···P, and one, two or three P···B/M linkages.
- At lowest M content each M has mostly M···B/P linkages, i.e. M···M linkages are uncommon.

As the M content increases:

- Some of the B becomes three-fold coordinated with P/M.
- Some of the P···P linkages are converted to P···M linkages.
- There is appearance and increase of M···M linkages.

It is useful to consider two additional factors influencing the connectivity. Firstly, the linkages expected in a randomly connected network can be predicted from probability theory. A bridging oxygen involves two bonds to B, P or M. Here we will consider bonds which are to P, which have a probability p, and bonds which are not to P, which have a probability $(1 - p)$. The values of p and $(1 - p)$ are the relative proportions of P–O bonds and B/M–O bonds respectively. The number of bonds of each type is given by the number of atoms multiplied by their coordination number. For the glass with low M content, the ratio of B:P:M is approximated by 1:4.5:1 and assuming coordination numbers of 4, 4 and 6 respectively, the value of $p = 0.64$ is obtained. For a random distribution, the different possible combinations of two bonds around a bridging oxygen are given by the binomial expansion:

$$(p + (1 - p))^2 = p^2 + 2p(1 - p) + (1 - p)^2 \qquad (10)$$

where p^2, $2p(1 - p)$ and $(1 - p)^2$ are the probabilities of bridging oxygen atoms in the form P–O–P, P–O–B/M and B/M–O–B/M respectively. For the glass with low M content this gives proportions of 0.40 for P···P, 0.49 for P···B/M and 0.11 for B/M···B/M linkages. Focusing on a given P in a randomly connected network, it would be expected that for every 1 P···B/M connection there would be 1.6 P···P connections (noting that the P···P are counted twice because they are common to 2 P). The NMR results indicate that a given P has 1 or less P···P linkage for every 1 P···B/M linkage, which indicates that P···P linkages are less preferred than P···B/M linkages. The linkages to non-bridging oxygen atoms, and thence to sodium atoms, have not been considered here, but if they were the overall result would be the same since the number of these linkages would be distributed evenly between the P, B and M and so the ratios would therefore remain the same.

The balance of bond valence at bridging oxygen atoms is a second factor that leads to a preference for P···B/M linkages over P···P linkages. Given that B has a valence of 3+ and a coordination of 4, the average bond valence of B–O is predicted to be 0.75. Similarly for P with a valence of 5+ and a coordination of 4, the average bond valence of P–O is 1.25. For M with a valence of 5+ and a coordination of 6, the average bond valence of M–O is 0.83. The P···B/M linkages provide well-balanced bond valence at bridging oxygen atoms as the sum of the P–O and the B–O or M–O bond valences is approximately equal to the bridging oxygen valence of 2−. Whereas P···P and B/M···B/M linkages have less-balanced bond valence. This may explain why there is a lower proportion of P···P linkages than expected for a randomly connected network.

Considering the glass with low M content, a good approximation to the composition is Na:B:P:M ratio of 5:1:4.5:1. Using the information gathered here it is possible to

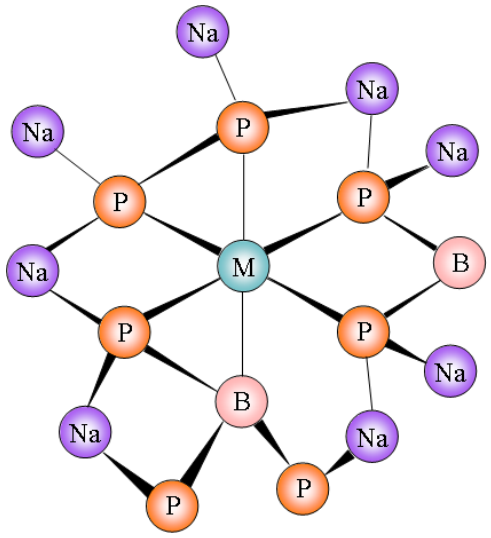

Figure 11. A model of the connectivity, the oxygen atoms are not shown but would be positioned on the lines between cations.

predict a model of the connectivity that serves as an example of how the components fit together. The typical connectivity of B could be described as 1 B having 3 B···P and 1 B···M linkages. The 4.5 P would have 3 B···P, 1.5 P···P (connecting two P), and 5 P···M linkages. This leads to 1 M having 1 M···B and 5 M···P linkages. The coordination of P would be completed with 7 bonds to O_{nb}. As the typical bond valence of a P–O bond is 1.25, the remaining bond valence on O_{nb} is 0.75. Thus the bond valence of 7 O_{nb} is balanced by 5 Na each with a valence of 1+. This model for connectivity is illustrated in figure 11.

The data shows that at higher M content the connectivity of the M changes so that it becomes chains and eventually each MO_6 octahedra is connected to several others. This is understandable considering the reduced availability of P and B. As the M concentration increases the relative amount of B and P decreases, therefore the relative number of B and P for linkages to each M decreases. At the same time, the P speciation changes such that there are less P–O–P links and more P–O–M links. The relative number of Na atoms, hence O_{nb}, available to each M also decreases significantly when the M content increases. Combining these effects it is seen that the M must become more linked with other M. Details of the structural effects which lead to clustering of MO_6 units can contribute to the explanation of the increase in third order non-linear susceptibility in these glasses at high M content.

5. Conclusions

This study has presented for the first time high energy x-ray diffraction, neutron diffraction and NMR data on the complex sodium niobium and sodium tantalum borophosphate glass system. Analysis of these results together with EXAFS and vibrational spectroscopy data provides sufficient information to construct a detailed picture of the glass structure. As expected, B and P play the role of tetrahedral network formers. At low M content (M = Nb/Ta) there are isolated MO_6 units with P···M and B···M linkages that contribute to the glass network. From bond valence considerations there is a preference for P···B/M over P···P linkages. In addition, P is coordinated to non-bridging oxygen atoms which are introduced by the presence of Na. As M content increases, so do the number of M···M linkages, leading first to corner sharing and then to each MO_6 unit being connected to several others. The behaviour of Nb is seen to be different to Ta in that Nb is off-centre in NbO_6 units at low Nb content, and the distortion of NbO_6 units increases with Nb content.

Acknowledgments

The authors wish to thank the EPSRC and STFC for funding, and the use of the EPSRC Chemical Database Service at the STFC Daresbury Laboratory. The Università di Cagliari is also acknowledged for funding under the project Fondo 5%. We would also like to thank Simon FitzGerald from Horiba for providing us with some of the Raman data. We are grateful for the help provided by Dr Frank Sowrey, Dr Mark Holland and Dr Philip Gunawidjaja.

References

[1] Vogel E M, Kosinski S G, Krol D M, Jackel J L, Friberg S R, Oliver M K and Powers J D 1989 Structural and optical study of silicate-glasses for nonlinear optical-devices *J. Non-Cryst. Solids* **107** 244–50

[2] Cardinal T, Fargin E, LeFlem G, Couzi M, Canioni L, Segonds P, Sarger L, Ducasse A and Adamietz F 1996 Non linear optical properties of some niobium(V) oxide glasses *Eur. J. Solid State Inorg. Chem.* **33** 597–605

[3] Dussauze M, Fargin E, Malakho A, Rodriguez V, Buffeteau T and Adamietz F 2006 Correlation of large SHG responses with structural characterization in borophosphate niobium glasses *Opt. Mater.* **28** 1417–22

[4] Nazabal V, Fargin E, Videau J J, Le Flem G, Le Calvez A, Montant S, Freysz E and Couzi M 1997 Second-harmonic generation of electrically poled borophosphate glasses: effects of introducing niobium or sodium oxides *J. Solid State Chem.* **133** 529–35

[5] Russo U, Lovisetto B, Marson S, Speghini A and Bettinelli M 2001 Mossbauer and optical spectroscopy of phosphoniobate and phosphotantalate glasses doped with iron *Phil. Mag.* B **81** 313–20

[6] Eljazouli A, Viala J C, Parent C, Leflem G and Hagenmuller P 1988 Structural investigation of glasses belonging to the Na2o-Nb2o5-P2o5 system *J. Solid State Chem.* **73** 433–9

[7] Cardinal T, Fargin E, Le Flem G and Leboiteux S 1997 Correlations between structural properties of Nb_2O_5–$NaPO_3$–$Na_2B_4O_7$ glasses and non-linear optical activities *J. Non-Cryst. Solids* **222** 228–34

[8] Malakho A, Dussauze M, Fargin E, Lazoryak B, Rodriguez V and Adamietz F 2005 Crystallization and second harmonic generation in thermally poled niobium borophosphate glasses *J. Solid State Chem.* **178** 1888–97

[9] Flambard A, Montagne L, Delevoye L, Palavit G, Amoureux J P and Videau J J 2003 Solid-state NMR study of mixed network sodium–niobium phosphate glasses *PNCS: 10th Int. Conf. on the Physics of Non-Crystalline Solids* (Parma: Elsevier Science) pp 75–9

[10] Soper A K, Howells W S and Hannon A C 1989 *ATLAS—Analysis of Time-of-Flight Diffraction Data from Liquid and Amorphous Samples* Rutherford Appleton Laboratory (RAL-89-046)

[11] Moss R M, Pickup D M, Hannon A C and Newport R J 2009 NXFit—Optimisation of structural parameters for combined x-ray and neutron diffraction data of disordered materials University of Kent private communication
[12] Tomic S, Searle B G, Wander A, Harrison N M, Dent A J, Mosselmans J F W and Inglesfield J E 2004 *New Tools for the Analysis of EXAFS: The DL_EXCURV Package* CCLRC ISSN 1362-0207
[13] Leclaire A, Borel M M, Grandin A and Raveau B 1994 The phosphoniobate RBNB2PO8—an ordered substitution of PO4 tetrahedra for NBO6 octahedra in the HTB structure *J. Solid State Chem.* **110** 256–63
[14] Brese N E and Okeeffe M 1991 Bond-valence parameters for solids *Acta Crystallogr.* B **47** 192–7
[15] Francisco M S P, Landers R and Gushikem Y 2004 Local order structure and surface acidity properties of a Nb_2O_5/SiO_2 mixed oxide prepared by the sol–gel processing method *J. Solid State Chem.* **177** 2432–9
[16] Bouchet R, Weibel A, Knauth P, Mountjoy G and Chadwick A V 2003 EXAFS study of dopant segregation (Zn, Nb) in nanocrystalline anatase (TiO_2) *Chem. Mater.* **15** 4996–5002
[17] Tanaka T, Yoshida T, Yoshida H, Aritani H, Funabiki T, Yoshida S, Jehng J M and Wachs I E 1995 XAFS study of niobium oxide on alumina *2nd Int. Symp. on Niobium Compounds* (Tokyo: Elsevier Science) pp 71–8
[18] Qiu D, Guerry P, Ahmed I, Pickup D M, Carta D, Knowles J C, Smith M E and Newport R J 2008 A high-energy x-ray diffraction, P-31 and B-11 solid-state NMR study of the structure of aged sodium borophosphate glasses *Mater. Chem. Phys.* **111** 455–62
[19] Hannon A C and Holland D 2006 A parameterisation for the composition dependence of N-4 in borate glasses *Phys. Chem. Glasses—Eur. J. Glass Sci. Technol.* B **47** 449–54
[20] Du J and Cormack A N 2005 The medium range structure of sodium silicate glasses: a molecular dynamics simulation (vol 349, pg 66, 2004) *J. Non-Cryst. Solids* **351** 956